

Unstable mass-outflows in geometrically thick accretion flows around black holes

Toru Okuda¹ * and Santabrata Das² †

¹ *Nishi-Asahioka-Cho 3-15-1, Hakodate 042-0915, Hokkaido, Japan*

² *Indian Institute of Technology Guwahati, Guwahati, 781039, India*

Accepted

ABSTRACT

Accretion flows around black holes generally result in mass-outflows that exhibit irregular behavior quite often. Using 2D time-dependent hydrodynamical calculations, we show that the mass-outflow is unstable in the cases of thick accretion flows such as the low angular momentum accretion flow and the advection-dominated accretion flow. For the low angular momentum flow, the inward accreting matter on the equatorial plane interacts with the outflowing gas along the rotational axis and the centrifugally supported oblique shock is formed at the interface of both the flows, when the viscosity parameter α is as small as $\alpha \leq 10^{-3}$. The hot and rarefied blobs, which result in the eruptive mass-outflow, are generated in the inner shocked region and grow up toward the outer boundary. The advection-dominated accretion flow attains finally in the form of a torus disc with the inner edge of the disc at $3R_g \leq r \leq 6R_g$ and the center at $6R_g \leq r \leq 10R_g$, and a series of hot blobs is intermittently formed near the inner edge of the torus and grows up along the outer surface of the torus. As a result, the luminosity and the mass-outflow rate are modulated irregularly where the luminosity is enhanced by 10–40% and the mass-outflow rate is increased by a factor of few up to ten. We interpret the unstable nature of the outflow to be due to the Kelvin-Helmholtz instability, examining the Richardson number for the Kelvin-Helmholtz criterion in the inner region of the flow. We propose that the flare phenomena of Sgr A* may be induced by the unstable mass-outflow as is found in this work.

Key words: accretion, accretion discs – black hole physics – hydrodynamics – Galaxy: centre.

1 INTRODUCTION

The observations as well as numerical simulations around black holes demonstrate regular, irregular and/or chaotic time variation of emergent radiations and mass-outflows over a wide range of time scales. The origins of such variable emissions and mass-outflows from the vicinity of the black holes are also numerous. The accretion luminosity depends on the adopted accretion models and its accretion rates. When the accretion rate is not too high, the luminosity is directly proportional to the accretion rate and can be described successfully by the standard thin-disc model (Shakura-Sunyaev, hereafter S-S, model) (Shakura & Sunyaev 1973). The standard model have been proven to be successful in studying the cataclysmic variables and later for neutron stars and black holes. However, for highly luminous accretion discs whose luminosity exceeds

the Eddington luminosity as is found in the black hole candidate SS 433 or for very low luminous discs compared with the predicted accretion rate as the case of the supermassive black hole candidate Sgr A*, the S-S model is not valid and alternative thick disc models, such as the slim disc model (Abramowicz et al. 1988), the advection-dominated accretion disc model (Narayan & Yi 1994, 1995) and the low angular momentum disc model (Mościbrodzka, Das & Czerny 2006; Czerny & Mościbrodzka 2008), have been developed.

Numerous studies of the hot thick accretion flow around the black holes have been carried out both theoretically and numerically to promote the insights of the black hole physics. One of the important results of the hot accretion flows is that the inflow and outflow rates in the accretion flow follow a power-law function of radius. To explain the inflow-outflow rate versus radius relation, two types of models of the adiabatic inflow-outflow solution (Blandford & Begelman 1999, 2004; Begelman 2012) and the convection-dominated accretion flow model (Narayan, Igumenshchev & Abramowicz 2000; Quataert & Gruzinov 2000; Abramowicz et al. 2002;

* E-mail: bbnbh669@ybb.ne.jp

† E-mail: sbdas@iitg.ernet.in

Igumenshchev 2002) have been proposed. Furthermore, the recent hydrodynamical (HD) and magneto-hydrodynamical (MHD) simulations result in new findings of such outflows, winds and jets in the field of hot accretion flows around the black holes (Narayan et al. 2012; Yuan, Bu & Wu 2012; Yuan, Wu & Bu 2012; Bu et al. 2013; Li, Ostriker & Sunyaev 2013; Yuan et al. 2015). The details of the geometrically thick hot accretion flows are referred to Yuan (2011) and Yuan & Narayan (2014).

The hot accretion flows show unstable behaviors of the outflows in most cases of the time-dependent numerical simulations. We have examined the thick accretion flows with low angular momentum and found that the outflows from the outermost boundary are always unstable, accompanying irregularly eruptive mass ejections (Okuda & Molteni 2012; Okuda 2014). Although we interpreted the unstable mass-outflow to be induced by the irregular radial oscillations of the centrifugally supported shock, the intrinsic origin of the unstable nature of mass-outflows is still an open question. In this paper, focusing on the outflows from the hot accretion flow, we examine the unstable nature of the outflows in terms of the Kelvin-Helmholtz instability, using time-dependent 2D hydrodynamical simulations. Finally, following the results of the unstable mass-outflow, we suggest a possible model which may explain the flaring events of Sgr A*.

2 NUMERICAL METHODS

2.1 Basic equations

We consider a supermassive black hole with mass $M = 4 \times 10^6 M_\odot$ which is estimated for the supermassive black hole candidate Sgr A*. We also assume a two-temperature plasma with ions being much hotter than electrons. The accreting gas is assumed to be very rarefied and optically thin. The set of relevant time-dependent equations is given in the spherical polar coordinates (r, ζ, φ) :

$$\frac{\partial \rho}{\partial t} + \text{div}(\rho \mathbf{v}) = 0, \quad (1)$$

$$\begin{aligned} \frac{\partial(\rho v)}{\partial t} + \text{div}(\rho v \mathbf{v}) &= \rho \left[\frac{w^2}{r} + \frac{v_\varphi^2}{r} - \frac{GM}{(r - R_g)^2} \right] - \frac{\partial p}{\partial r} \\ &+ \text{div}(\mathbf{S}_r) + \frac{1}{r} S_{rr}, \end{aligned} \quad (2)$$

$$\frac{\partial(\rho r w)}{\partial t} + \text{div}(\rho r w \mathbf{v}) = -\rho v_\varphi^2 \tan \zeta - \frac{\partial p}{\partial \zeta} + \text{div}(r \mathbf{S}_\zeta) + S_{\varphi\varphi} \tan \zeta, \quad (3)$$

$$\frac{\partial(\rho r \cos \zeta v_\varphi)}{\partial t} + \text{div}(\rho r \cos \zeta v_\varphi \mathbf{v}) = \text{div}(r \cos \zeta \mathbf{S}_\varphi), \quad (4)$$

$$\frac{\partial \rho \varepsilon_i}{\partial t} + \text{div}(\rho \varepsilon_i \mathbf{v}) = -p_i \text{div} \mathbf{v} + \Phi - q^{\text{ie}} \quad (5)$$

and

$$\frac{\partial \rho \varepsilon_e}{\partial t} + \text{div}(\rho \varepsilon_e \mathbf{v}) = -p_e \text{div} \mathbf{v} + q^{\text{ie}} - q_{\text{syn}} - q_{\text{br}}, \quad (6)$$

where $\mathbf{v} = (v, w, v_\varphi)$ are the three velocity components, ρ is the density, ε_i and ε_e are the specific internal energies of the ion and electron, p_i and p_e are the gas pressures of the ion and electron, $\mathbf{S} = (\mathbf{S}_r, \mathbf{S}_\zeta, \mathbf{S}_\varphi)$ denotes the viscous stress tensor and $\Phi = (\mathbf{S} \cdot \nabla) \mathbf{v}$ is the viscous dissipation rate per unit mass. The full expression of the viscous stress tensor \mathbf{S} and the dissipation rate Φ are given in

Okuda, Fujita & Sakashita (1997). Here, the kinematic viscosity ν is given by

$$\nu = \alpha c_s \min [H_p, H], \quad (7)$$

where c_s , H_p and H are the local sound speed, the pressure scale height and the disc thickness, respectively, and α is a dimensionless viscosity parameter which is usually taken to be in the range $10^{-3} \leq \alpha < 1$. The pseudo-Newtonian potential is adopted in the momentum equation. q^{ie} , q_{br} and q_{syn} are the energy transfer rate from ions to electrons by Coulomb collisions, the cooling rate of electrons by electron-ion and electron-electron bremsstrahlungs and the synchrotron cooling rate, respectively (Esin et al. 1996; Narayan & Yi 1995; Stepney & Guilbert 1983). In calculation of q_{syn} , we give the magnetic field B at each radius, assuming that the ratio β of the magnetic energy density to the thermal energy density is constant throughout the region. We neglect the radiation transport assuming that the flow is optically thin.

In the equations (5) and (6), we assume that all of the viscous dissipation energy is given to ions because an ion particle is much heavier than an electron particle and it is poorly known how the viscous dissipation energy is shared between the ions and electrons. However, as a representative case, we examined what result is obtained when half of the dissipation energy is shared to the electron and observed that the total luminosity is altered maximumly by a small factor of 1.5 due to the larger electron temperature in the intermediate region on the equator, although the mass-outflow rate is not altered largely. This indicates that the above assumption is reasonable for our present study.

Recent MHD simulations show that $r - \varphi$ component of the viscous stress is dominated over other components. However, we used the true kinematic viscous stress which includes all components of the stress, in expectation of enhancement of the outflow activity through the angular momentum transfer and the viscous dissipation. From some examinations of the effects of viscous stress components, we find that in both cases B and C the global features of the total luminosity and the mass-outflow rate are not altered largely even if only the $r - \varphi$ component of the stress is used.

In the present two-temperature plasma with the ion temperature T_i and the electron temperature T_e , the adiabatic indices for ions (γ_i) and electrons (γ_e) possess different values depending on their temperature states. In reality, we use γ_e is 1.6 for $kT_e \leq m_e c^2$, equivalently, $T_e \leq 5.9 \times 10^9 \text{K} (= T_c)$ where electrons are non-relativistic and γ_e is 4/3 for $kT_e \geq m_e c^2$ where electrons are relativistic. Here, T_c is the critical electron temperature at which electrons in the non-relativistic state change into the relativistic state. For ions, γ_i is taken to be 1.6 throughout the region because ions remain in a non-relativistic state of $kT_i \leq m_p c^2$ (Fukue 1986).

The set of partial differential equations (1)–(6) is numerically solved by a finite-difference method under adequate initial and boundary conditions. The numerical schemes used are basically the same as that described by (Okuda 2014). The methods are based on an explicit-implicit finite difference scheme.

2.2 Modeling of the thick accretion flow

We focus here on the geometrically thick and optically thin accretion discs. The low angular momentum flow and the advection-dominated accretion flow around the black holes belong to this category. Using the flow parameters of the thick accretion flow, we examine the time-dependent behaviors of the outflow which is ejected from the outer boundary. We consider three representative cases of the accretion flow with no angular momentum (case A), the low angular momentum flow (case B) and the advection-dominated accretion flow (case C), respectively. In the previous work, we have studied the low angular momentum flow model in the inviscid limit (Okuda & Molteni 2012; Okuda 2014) but we intend to re-examine here considering the effect of viscosity. The case A is studied for initial flow with flow parameters same as case B. For case C, we start with the self-similar solutions of the advection-dominated accretion flow (Narayan & Yi 1995; Yuan & Narayan 2014). Following this, the self-similar solutions are given by

$$v \approx -0.367 \alpha r^{-1/2}, \quad (8)$$

$$\lambda \approx 0.292 r^{1/2}, \quad (9)$$

$$c_s^2 \approx 0.156 r^{-1}, \quad (10)$$

$$\rho = 1.05 \times 10^{-4} \alpha^{-1} \dot{m}^{-1} \dot{m} r^{-3/2+s} \text{ g cm}^{-3}, \quad (11)$$

where λ is the specific angular momentum, s is the index parameter. Here, r is measured in units of the Schwarzschild radius R_g , v and c_s are measured in speed of light c and λ is given in units of cR_g . The mass of the black hole m and the accretion rate \dot{m} are expressed in unit of solar mass and the Eddington rate of $1.4 \times 10^{18} \text{ gm s}^{-1}$, respectively. In this self-similar solution, we consider a constant mass accretion rate with the index $s = 0$. Although recent HD simulations of the thick hot accretion flow over a wide range of $r \sim 10^4 R_g$ (Yuan, Wu & Bu 2012) reveal slightly different relations compared to the above self-similar solutions (i.e. $\rho \propto r^{-0.65}$ and $r^{-0.85}$ for $\alpha = 0.001$ and 0.01 , respectively), eventually it does not affect the present study of the mass-outflow. In Table 1, we show the flow parameters for cases A, B and C, where the flow variables at the outer disc boundary are illustrated. The electron temperatures at the outer boundary are approximately taken to be equal to the ion temperatures.

2.3 Initial and Boundary Conditions

The initial discs of cases B (also A) and C are given by 1D solutions of the low angular momentum accretion flow model (Okuda 2014) and the self-similar solutions (8)–(11) of the advection-dominated accretion flow, respectively. Furthermore, assuming the density distribution of $\rho \sim r^{-1}$, we construct an initial rarefied atmosphere around the discs to be approximately in radially hydrostatic equilibrium.

Physical variables at the inner boundary, except for the velocities, are given by extrapolation of the variables near the boundary. However, we impose limiting conditions that the radial velocities are given by a fixed free-fall velocity and the angular velocities are zero. On the rotational axis and the equatorial plane, the meridional tangential velocity w is zero, and all scalar variables must be symmetric relative to

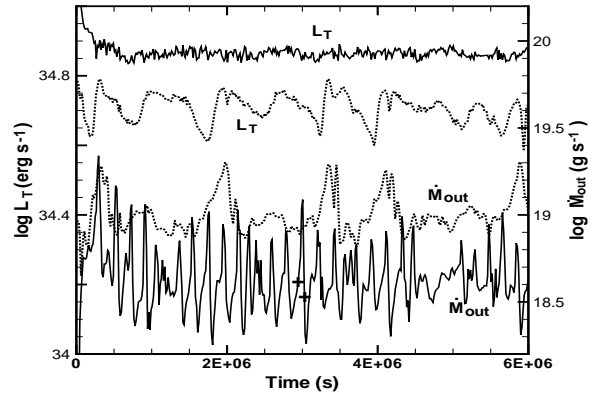


Figure 1. Time variations of total luminosity L_T (erg s^{-1}) and mass-outflow rate \dot{M}_{out} in case A with the viscosity parameter $\alpha = 0.0$ (solid lines) and 0.1 (dotted lines).

these axes. The outer boundary at $r = r_{\text{out}}$ is divided into two parts — one is the disc boundary through which matter is continuously entering from the outer disc with a constant accretion rate \dot{M} and the other is the outer boundary region above the accretion disc. We impose free-floating conditions on this outer boundary and allow matter to eject in the form of outflow where any inflow is prohibited. All flow variables at the outer boundary of the disc are kept constant always.

3 THE NUMERICAL RESULTS

3.1 The thick accretion flow with no angular momentum

Case A is the simplest case of thick accretion flows. The initial flow variables of case A are given by 1D solution of the low angular momentum flow model (case B) in Table 1 but the angular momentum is neglected here. After the time integration, the upstream accreting gas falls towards the gravitational center and soon reaches close to the inner edge of the disc. Though most of the accreting gas is primarily swallowed into the black hole, a part of the gas is ejected upward along the z -axis due to the high temperature near the inner edge. Since the ejected gas interacts with the downward accretion gas with considerable amount of horizontal velocity component, an oblique shock is formed along the z -axis and is elongated in the region of $z \sim 80R_g$ and $r \sim 30R_g$ at $t \sim 10^5$ s. Eventually, the upward moving gas in the shocked region is escaped from the outer boundary. As a result, a few to several percent of the input accreting matter is ejected through the outermost boundary.

Fig. 1 shows the time variations of the total luminosity L_T integrated in the computational domain V and mass-outflow rate \dot{M}_{out} ejected from the atmospheric outer boundary S for case A. Here, L_T and \dot{M}_{out} are given by

$$L_T = \int (q_{\text{br}} + q_{\text{syn}}) dV, \quad (12)$$

and

Table 1. Flow parameters as specific angular momentum λ , adiabatic index of ions γ_i , mass accretion rate \dot{M} ($M_\odot \text{ yr}^{-1}$), radial velocity v_{out} , density ρ , ion temperature T_i , relative disc thickness h/r , viscosity parameter α and ratio β of the magnetic energy density to the thermal energy density at $R_{\text{out}} = 200R_g$ in the two-temperature model.

case	λ	γ_i	\dot{M} ($M_\odot \text{ yr}^{-1}$)	$-v_{\text{out}}/c$	ρ	T_i (K)	h/r	α	β
A	0.0	1.6	4.0×10^{-6}	5.06×10^{-2}	5.61×10^{-19}	1.292×10^9	0.43	0.0–0.1	10^{-3}
B	1.35	1.6	4.0×10^{-6}	5.06×10^{-2}	5.61×10^{-19}	1.292×10^9	0.43	10^{-3} –0.01	10^{-3}
C	4.13	1.6	1.5×10^{-6}	2.60×10^{-2}	4.14×10^{-18}	2.082×10^9	0.50	10^{-3} –0.1	10^{-3}

$$\dot{M}_{\text{out}} = \int \rho_{\text{out}} \mathbf{v}_{\text{out}} d\mathcal{S}, \quad (13)$$

where the suffix ‘out’ shows the value at the atmospheric outer boundary. The solid and dotted lines represent the cases with $\alpha = 0.0$ and 0.1 , respectively. We find that the luminosities and the mass-outflow rates vary quite irregularly. In particular, the variation for first one is less than 20 % and for second one is by a factor of few. Here, the luminosities are mainly dominated by the bremsstrahlung emission. The mass-outflow rates increase with the increasing viscosity and conversely the luminosities decrease especially in the case of the maximum viscosity with $\alpha = 0.1$. Due to the viscous heating, ion temperature becomes higher and therefore, the shock wave near the z-axis is pushed outward. Hence, the outflow over the oblique shock is enhanced as seen in Fig. 2. On the other hand, the electron temperature behind the shock becomes lower when the shock is pushed away. As the dominant energy emission process is due to the free-free emission which mostly depends on the electron temperature behind the shock, the luminosity eventually becomes lower by a small factor.

We wonder why the mass-outflow rates are considerably modulated chaotically in spite of the small modulations of the luminosity. To understand the outflow activity, it is useful to follow the animation of the time-dependent density and temperature contours. Fig. 2 shows the snapshots of the animation over a typical cycle in the time variation of the mass-outflow rate, where the temperature contours at $t/10^6 = 2.899, 2.929, 2.960, 2.990, 3.005$ and 3.036 s are shown. The large mass-outflow activity begins at the elongated region of the shocked surface. Firstly, a hot and rarefied blob with small size is formed at the upper edge ($z \sim 80$ and $r \sim 40$) of the shocked region. The hot blob grows up in the outward direction and starts disintegrating into several small blobs. Ultimately, these blobs further continue to expand outward. The maximum mass-outflow rate is attained at the time of Fig. 2(d). Thus, the unstable mass-outflow is observed even in the case of the thick accretion flow with no angular momentum.

3.2 The low angular momentum accretion flow

The low angular momentum accretion flows without viscosity were examined in the previous works (Okuda & Molteni 2012; Okuda 2014). Using same sets of the model parameters of the specific angular momentum λ and the specific total energy ϵ which were estimated from the analysis of stellar wind of nearby stars around Sgr A* (Czerny & Mościbrodzka 2008; Mościbrodzka, Das & Czerny 2006), we showed that the irregularly oscillating shocks are formed in the inner re-

gion and consequently the luminosity and mass-outflow rate are modulated within a factor of few and several, respectively. In this work, we study the low angular momentum flow model including viscosity and observe that the characteristics of the low angular momentum flow are not altered largely compared to the inviscid flow, when viscosity parameter α is small as $\sim 10^{-3}$. Similarly to case A, an oblique shock surface is formed due to the interactions between the upward moving gas and the downward accreting gas. Since the flow is rotating around the z-axis, the shock surface on the equatorial plane is pushed away in the outward direction due to the centrifugal force and is oscillated irregularly at $r/R_g \sim 20 - 50$. During shock oscillations, a small hot blob is occurred in the shocked region near the equatorial plane, grows upward, undergoes to become maximal at the upper edge of the shocked region and finally attains the outer boundary. The evaluation of this hot blob seems to be suitable to explain the episodic mass-outflow activity.

Fig. 3 represents the time variations of the total luminosity $L_T \text{ erg s}^{-1}$, the mass-outflow rate \dot{M}_{out} , the mass-inflow rate \dot{M}_{in} at the inner edge and the shock position R_s/R_g on the equatorial plane for case B with $\alpha = 10^{-3}$. The mass-outflow rate attains 10 % of the input accretion rate and varies by a factor of 2 – 3 whereas the luminosity is modulated by a factor of 1.5. The shock position on the equatorial plane oscillates irregularly around $r \sim 35R_g$. The large mass-outflow activity occurs roughly in regular intervals of the order of few days. Fig. 4 shows the contours of ion temperature T_i at $t = 1.83 \times 10^6$ s for case B with $\alpha = 10^{-3}$. The time is indicated by ‘+’ on the curve \dot{M}_{out} in Fig. 3. The shock surface is illustrated by the black thick lines which are located at $r \sim 35 R_g$ on the equatorial plane and is elongated obliquely. The rarefied hot funnel region is shown by the red zone along the z-axis.

On the other hand, when α is as large as 0.1, the shock wave formed initially in the inner region that expands outward and finally disappears from the outer boundary. At the later phases, a large scale convective motion is prevailed in the entire accretion flow. As a result, most of the input accreting matter is ejected from the outer boundary and the mass-outflow rate is modulated by a factor of few.

3.3 The advection-dominated accretion flow

Although the initial flow variables of case C are obtained by the self-similar solution of the advection-dominated flow, the evolution of the flow at the initial state is similar to that of case B. The upstream accreting gas falls towards the gravitational center and the outflows are generated from the surrounding region of the inner edge. These outflowing gas interacts with the downward accreting gas, resulting in

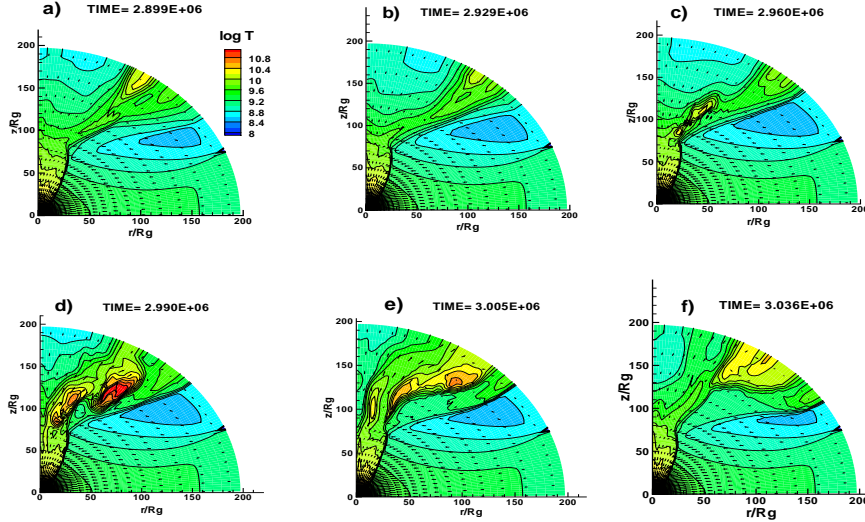


Figure 2. Subsequent snapshots of temperature contours at phases of $t/10^6 = 2.899, 2.929, 2.960, 2.990, 3.005$ and 3.036 (s) during an eruptive mass ejection in the curve of \dot{M}_{out} with $\alpha = 0.0$ of Fig. 1. The phases of the snapshots (a) and (f) are shown by two crosses in the solid line \dot{M}_{out} of Fig. 1

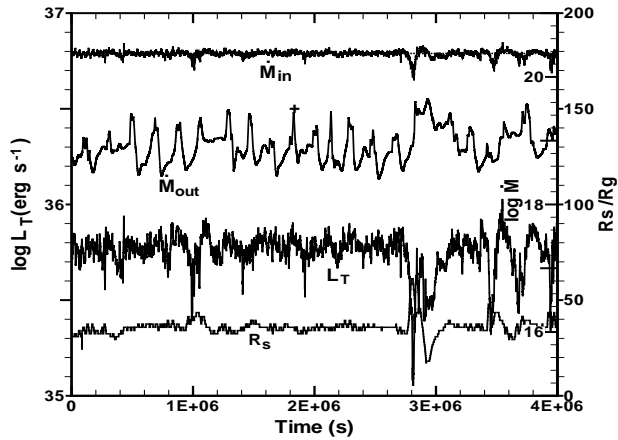


Figure 3. Time variations of total luminosity L_T (erg s^{-1}), mass-outflow rate \dot{M}_{out} (gm s^{-1}), mass-inflow rate \dot{M}_{in} at the inner edge and shock position R_s/R_g on the equatorial plane for case B with $\alpha = 10^{-3}$.

the formation of oblique shock. However, since the flow has larger angular momentum than that in case B, the shock on the equatorial plane continues to move outward gradually and finally reaches the outer disc boundary. As a result, the phenomenon of shock formation is never recovered. After a long integration time more than ~ 100 orbital period at the outer boundary, the entire flow seems to settle down in a steady state, although the luminosity is still modulated by a very small factor. On the other hand, the mass-outflow rate remains as large as 10% of the input accretion rate and varies by a factor of ten or so.

Fig. 5 shows the time variations of the total luminosity

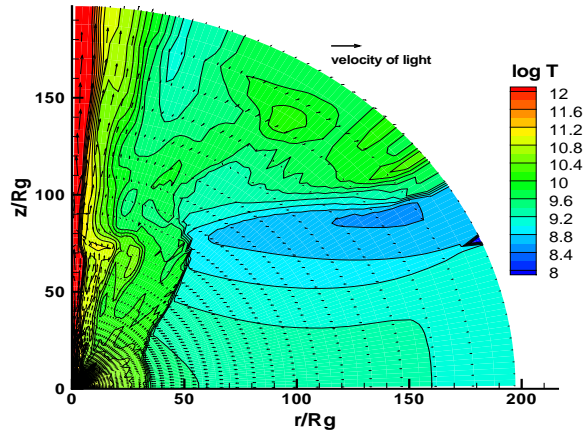


Figure 4. Contours of ion temperature T_i with velocity vectors at $t = 1.83 \times 10^6$ s of case B with $\alpha = 10^{-3}$. The evolutionary phase is denoted by '+' in the curve \dot{M}_{out} of Fig. 3. The velocity of light is indicated by the upper arrow.

L_T erg s^{-1} and the mass-outflow rate \dot{M}_{out} g s^{-1} for case C with $\alpha = 0.1$. In the plot, dashed horizontal line denotes the input accretion rate $\sim 10^{20}$ g s^{-1} . It should be noticed here that the mass-outflow ejected from the outer boundary surface with the polar angle $\zeta \geq 60^\circ$ is presented in Fig. 5 due to the following reason. We imposed free-floating conditions on the outer atmospheric boundary which allow only for outflowing matter. However, recent HD simulations of the hot accretion flow on large scales, namely, from the black hole horizon to 10 Bondi radius (Li, Ostriker & Sunyaev 2013) indicate that the above boundary conditions may be invalid. This is because convective motions prevail even in the outer

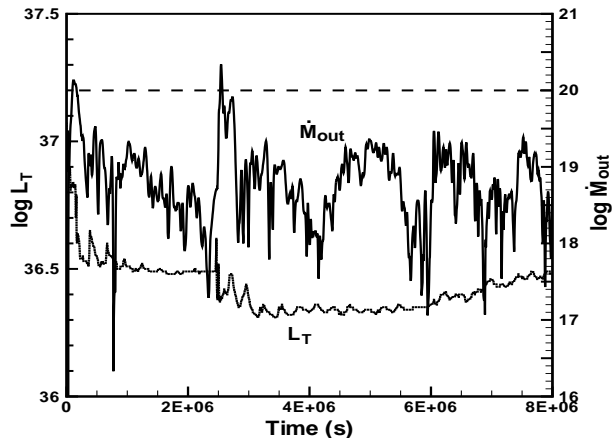


Figure 5. Time variations of total luminosity L_T (erg s^{-1}) and mass-outflow rate \dot{M}_{out} in case C with $\alpha = 0.1$, where the dashed horizontal line denotes the input accretion rate.

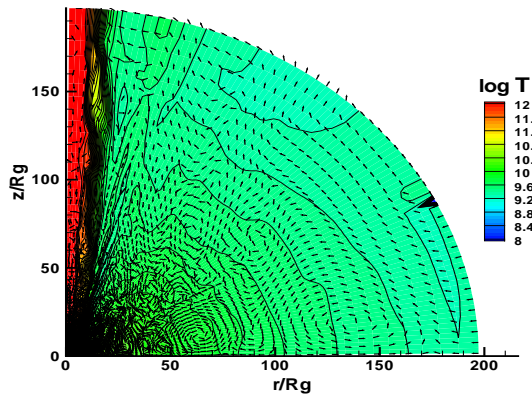


Figure 7. Same as Fig. 6 but for the ion temperature T_i with unit velocity vectors, where many convective cells are found in the inner region.

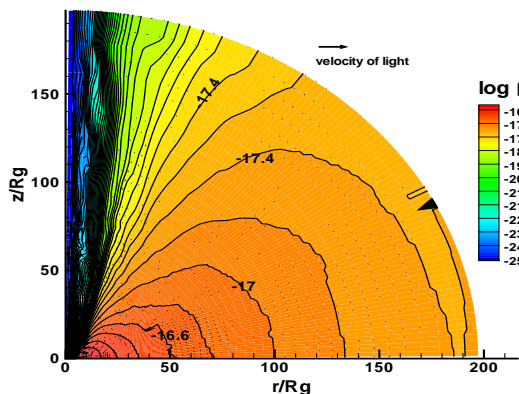


Figure 6. Contours of density ρ (g cm^{-3}) and velocity vectors at $t = 5.0 \times 10^6$ (s) for case C. The velocity of light is indicated by the upper arrow.

boundary region used in our simulations and accordingly there may exist outer flows with not only positive velocities but also negative ones at the outer boundary. On contrary, the boundary conditions adopted in this work seems to be justified in the polar region with $\zeta \geq 60^\circ$, where the high velocity jets with only positive radial velocities appear in this conical region.

In Fig. 6, we present the contours of the density at $t = 5.0 \times 10^6$ s for case C with $\alpha = 0.1$. The corresponding contours of ion temperature are depicted in Fig. 7, where the velocity vectors are given by unit vectors. Here we find that the flow is unstable against convection and many convective cells are found in the inner region. It is remarkable that a torus disc with an inner edge of $r \sim 3R_g$ and a concentric center at $r \sim 6R_g$ is formed in the advection-dominated accretion flow.

In Fig. 8, we show the variations of density ρ , ion temperature T_i , electron temperature T_e and radial velocity v on the equatorial plane as function of radial coordinate. Note

that the density and the temperatures on the equator have their maximum values at $r \sim 6R_g$ and decrease sharply inward. At $r \sim 3R_g$, the temperatures start increasing discontinuously although density continues to decrease even further. In Fig. 9, we zoom the inner edge of the torus disc to represent the contours of density with velocity vectors at the same phase as Figs. 6 and 7 for clarity. It is clear from the figures that the torus disc with the center at $r \sim 6R_g$ has the inner edge of the disc at $r \sim 3R_g$. We observe that the outflow begins at $r \sim 3R_g$ on the equator and goes up along the outer surface of the torus disc. In the region $r < 3R_g$, the gas falls toward the black hole and the density at the torus edge becomes very small and the flow has a discontinuous surface of the temperature there.

In order to understand the irregular oscillation of mass-outflow, we examine the time-dependent animations of density and temperature contours with velocity vectors. Then, we notice the formation of a series of hot blobs near the inner edge of the torus and their subsequent evolution along the outer surface of the torus. These hot blobs are originated in the innermost region between the inner edge ($r/R_g \sim 3$) of the torus disc and the inner edge ($r/R_g = 1.5$) of the flow.

We examine another case with $\alpha = 10^{-3}$ for the advection-dominated accretion flow. In this case, we again find the similar results as seen for $\alpha = 0.1$, i.e., the large modulation of the mass-outflow rate, the small modulation of the luminosity and the torus disc formation. The mass-outflow rate varies irregularly by more than a factor of ten and roughly occurs in every several hours. A series of hot blobs is also generated in the innermost region and grows up along the boundary zone between the outflow and the outer surface of the disc. The torus disc has the center at $r \sim 10R_g$ and the inner edge of the disc at $r \sim 6R_g$. The total luminosity is obtained as $\sim 10^{37}$ erg s^{-1} which is one order of magnitude larger than the case with $\alpha = 0.1$. This is due to the fact that the input density at the outer boundary is much larger as seen from equation (11).

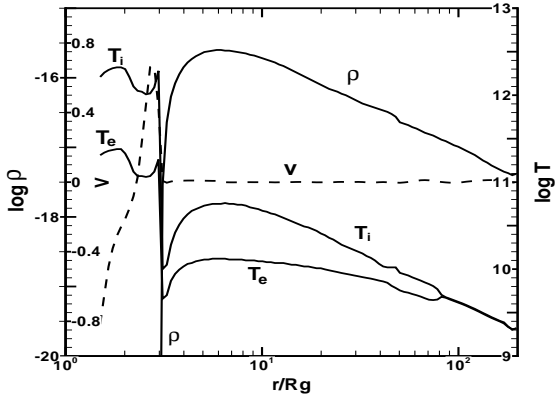


Figure 8. Variations of density ρ (g cm^{-3}), ion temperature T_i , electron temperature T_e and radial velocity v on the equatorial plane as observed in case C.

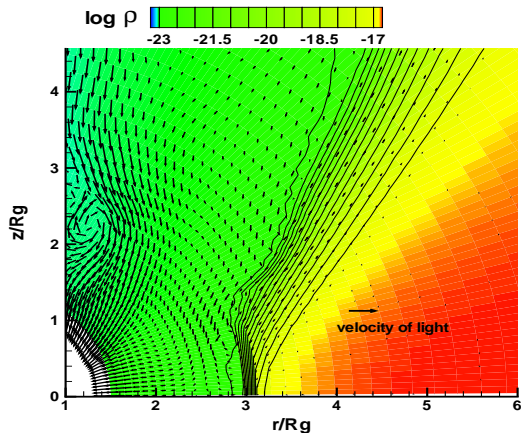


Figure 9. Same as Fig. 6, but near the inner edge, where at $r \sim 3R_g$ the mass-outflow begins upward along the disc surface.

4 KELVIN-HELMHOLTZ INSTABILITY AS THE ORIGIN OF THE UNSTABLE NATURE OF THE OUTFLOWS

We have examined that the mass-outflows in the geometrical thick accretion flows such as cases A, B and C are generally unstable and the mass-outflow rates vary by more than a factor of few up to ten. In cases of A and B, the apparent origin of the outflow activity is ascribed to the formation of hot blobs and its evolution toward the outer boundary. We have examined such modulations of the mass-outflow rate in other simulations of 2D rotating accretion flows around a stellar-mass ($10M_\odot$) and a supermassive (10^6M_\odot) black holes over a wide range of input accretion rates as $10^{-7} \leq \dot{M}/\dot{M}_E \leq 10^{-4}$ (Okuda, Teresi & Molteni 2009). In addition, examining 2D simulations for the disc of SS 433 at super-Eddington luminosities, we found remarkable modulations of the accretion rate near the inner edge that results in the formation of recurrent hot blobs with high temperatures and low densities at the disc plane. Based on this observation, we proposed that this may explain the massive

jet ejection as well as the QPOs phenomena observed in SS 433 (Okuda, Lipunova & Molteni 2009).

What is the intrinsic origin of the unstable nature of the outflows which is relevant to the hot blobs? In this respect, we consider shear instability or Kelvin-Helmholtz instability that may lead to the hot blobs and the winding waves of density. The shear instability and the Kelvin-Helmholtz instability can generally occur when there exists a velocity shear in a single continuous fluid or if there is a velocity difference across the interface between two fluids. Finally, the theory predicts the onset of instability and transition to the turbulent flow in fluids of different densities moving at various speeds (Chandrasekhar 1961). Certainly, in cases A and B, there exists an interface between the outgoing flow and the downward accreting gas as the shock surface with discontinuous velocities and densities and the hot blobs are formed along this interface and are evolved toward the upper shocked region. For case C, the hot blobs exist along the interface between the outflow and the outer surface of the torus disc. Therefore, the Kelvin-Helmholtz instability generated at the interface may be developed into the hot blobs and the winding waves.

For the sake of simplicity, let us consider an extreme type of stratification, namely a plane parallel two-layer system in which a layer of fluid with velocity v_1 and density ρ_1 floats over another layer with velocity v_2 and density ρ_2 where a gravitational force g acts vertically to the layers. Then, gravity waves propagate through the interface separating the two layers and grow in time. This leads to overturning in the vicinity of the interface and mixing over a height δH along the z -axis vertical to the layers, which is called the Kelvin-Helmholtz instability. In this simple picture, the growth of the Kelvin-Helmholtz instability is determined by a criterion of Richardson number (Chandrasekhar 1961; Shu 1992),

$$R_i \equiv \frac{-g(d\rho/dz)}{\rho(dv/dz)^2} < \frac{1}{4}. \quad (14)$$

Then, we have the Richardson number approximately as

$$R_i \simeq \frac{-g\delta H |\rho_2 - \rho_1|}{\bar{\rho}(v_2 - v_1)^2}. \quad (15)$$

In Fig. 2, we find the oblique shock front present in the accretion flow. Regarding the shock front and δH as the interface mentioned above and the shock thickness, respectively, we estimate the Richardson number. Across the interface, if the velocity difference parallel to the shock surface is not large enough, the criterion described in Eq. (14) is never satisfied. Fig. 10 illustrates the shock surface (thick line) as in Fig. 2 and the geometry of the shock front with thickness δH where $S(r, \zeta)$ and $T(r, \zeta + \delta\zeta)$ are the intersection points of the shock front with a circle of radius r centered at the origin, ω is the angle between the gravitational force direction and the tangent to the shock surface at point S, η is the angle between the tangent at point S and x -axis. With this, the Richardson number in units of the Schwarzschild radius and the speed of light is given by,

$$R_i \simeq \frac{1}{2} \frac{|\rho_2 - \rho_1|}{\bar{\rho}} \frac{\delta\zeta \sin \omega \cos(\omega - \frac{\delta\zeta}{2})}{r (v_2 - v_1)^2}, \quad (16)$$

where v_1 and v_2 are the components of pre-shock and post-shock velocities parallel to the tangent at S. The physical

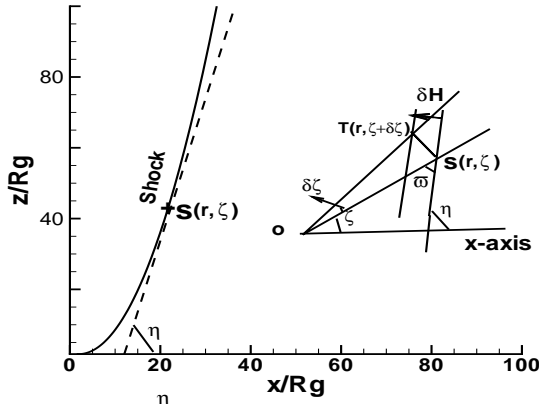


Figure 10. Geometry of shock surface with shock front thickness δH found in Fig. 2, where $S(r, \zeta)$ and $T(r, \zeta + \delta\zeta)$ are the intersection points of the shock front with a circle of radius r centered at the origin, ω is the angle between the gravitational force direction and the tangent to the shock surface at point S , η is the angle between the tangent at the point S and x -axis.

variables at the points S and T are determined approximately from the numerical data of the flow. As an example, we take a point on the shock front in Fig. 2a., whose radius is $67.4R_g$. For this point, in Fig. 11, we show the variation of density ρ , radial velocity v_r and azimuthal velocity v_ϕ as function of polar angle ζ measured from the equatorial plane. The shock transition is found here in the region of $63.9^\circ \leq \zeta \leq 67.5^\circ$ and $\delta\zeta \sim 3.6^\circ$. From the numerical data, furthermore, we know $\rho_1, \rho_2, (v_r)_1, (v_r)_2, (v_\phi)_1, (v_\phi)_2, \omega (= \eta - \zeta), v_1 = (v_r)_1 \cos \omega + (v_\zeta)_1 \sin \omega, v_2 = (v_r)_2 \cos(\omega - \delta\zeta) + (v_\zeta)_2 \sin(\omega - \delta\zeta)$ and finally estimate R_i . For case C, we do not find the shock interface found in cases A and B. However, there exists a discontinuous boundary zone between the torus disc and the outflowing gas where change of temperature and velocities occur very sharply as observed in Figs. 8 and 9. We apply the above method at this boundary zone to obtain the Richardson number.

In Fig. 12, we plot the distribution of the Richardson number R_i as a function of radial distance r/R_g obtained for the oblique shocks in Fig. 2(a) of case A (open squares) and in Fig. 4 of case B (diamonds), and for the boundary zone around the torus disc as in Fig. 9 of case C (closed circles). This shows that the criterion (Eq. 14) for Kelvin-Helmholtz instability is not satisfied near the equatorial plane but is established apart from the equator for all cases. This suggests that the unstable property of the outflows would possibly be ascribed to the Kelvin-Helmholtz instability.

5 A POSSIBLE MODEL TO THE FLARES OF SGR A*

The supermassive black hole candidate Sgr A* possesses a quiescent state and a flare state. The flares of Sgr A* have been detected in multiple wavebands from radio, sub-millimetre, IR to X-ray. The unstable mass-outflow activities examined in this work demonstrate both small and large amplitude modulations of the total luminosity and the mass-

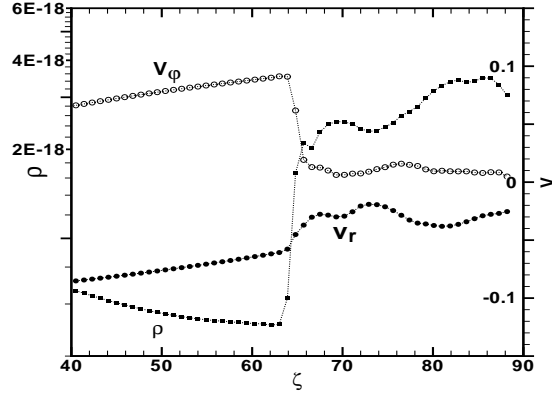


Figure 11. Plot of density ρ (g cm^{-3}), radial velocity v_r and azimuthal velocity v_ϕ as function of polar angle ζ at $r/R_g = 67.4$ on the shock front in Fig. 2a, where the shock transition is found in the region of $63.9^\circ \leq \zeta \leq 67.5^\circ$ and $\delta\zeta \sim 3.6^\circ$.

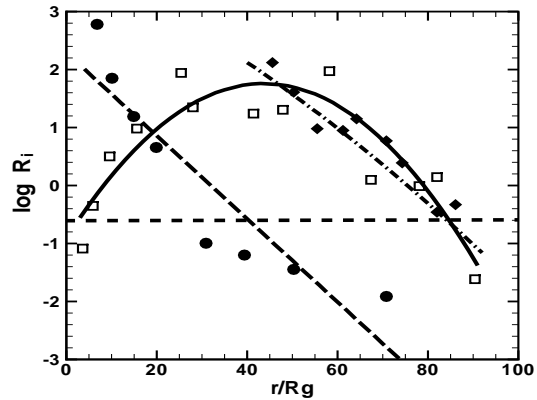


Figure 12. Variation of the Richardson number R_i as function of radius on the shock surface in Fig. 2(a) of case A (open squares), in Fig. 4 of case B (diamonds) and on the boundary zone around the torus disc in Fig. 9 of case C (circles). The corresponding fitted curves are shown by thick solid, dash-dotted and long-dashed lines, respectively. The horizontal dashed line denotes the critical value $R_i^{cr} = 0.25$ for the Kelvin-Helmholtz instability.

outflow rate which seems to be relevant for explaining the flaring phenomena observed in Sgr A*. The total luminosity found in cases B and C satisfactorily explains the existence of low luminosity of $\sim 10^{36}$ erg s^{-1} for Sgr A*. Similarly, the irregularly eruptive mass-outflows may correspond to the flare activities of Sgr A*.

The observations of Sgr A* show that the duration of the X-ray and IR flares are typically of 1-3 hours and the flare events usually occurs few times per day. In the simulation of cases B and C, we find that the duration and the interval between the successive eruptive mass-outflows roughly are in agreement with the flares of Sgr A*. But, the small modulations of luminosity does not correspond to the large amplitudes of the flare intensities observed at various wavelengths, because the amplitudes at radio,

IR and X-ray are roughly varied by factors of 1/2, 1-5 and 45, respectively (Genzel et al. 2003; Ghez et al. 2004; Eckart et al. 2006; Meyer et al. 2006a,b; Trippe et al. 2007; Yusef-Zadeh et al. 2009, 2011). It is well known that the sub-millimeter flare lags the X-ray flare roughly by two hours. From these facts, we propose a possible model of the unstable mass-outflow applicable to the flare phenomena of Sgr A*. This is basically a scenario of the temporal sequence of disc-jet coupling observed in the X-rays, IRs and radio wavelengths of the microquasar GRS 1915+105 (Mirabel et al. 1998). Here, we consider that the total emission in our models corresponds to the permanent emission of the quiescent state of Sgr A*, whereas only the emission of Sgr A* flare is produced at the distant region far away from the Sgr A* through the interaction between the surrounding dense interstellar matter and the high-velocity jets. These jets are originated in the unstable mass-outflows as examined here. The ejected wind carries sufficient outflowing mass of rate $\sim 10^{19} - 10^{20} \text{ g s}^{-1}$ and a total kinematic energy of $\sim 10^{36} - 10^{37} \text{ erg s}^{-1}$ to reproduce the flare phenomena. However, one needs to incorporate other mechanisms also so that the high-velocity wind could be accelerated up to the relativistic speed. This is because the outflow velocities at the outer boundary in cases B and C are limited to sub-relativistic regime as $\sim 0.01 - 0.1c$.

When we consider the flare activities of Sgr A*, it is required for us to treat MHD model because it is widely believed that the existence of the magnetic field is inevitable from the spectral analyses of Sgr A* and that magnetic turbulence induced by magneto-rotational instability is responsible for the angular momentum transfer. In this respect, by analogy with the coronal mass ejection on the Sun, Youan et al. (2009) proposed a MHD model for the formation of episodic jets from black holes associated with the closed magnetic fields in an accretion flow. In their model, shear and turbulence of the accretion flow deform the field and result in the formation of a flux rope in the corona and the flux rope is ejected through the magnetic reconnection process in a current sheet under the magnetic field.

Although the unstable outflows examined here are restricted to the non-magnetized accretion flow, we notice that the comparative studies of 2D hydrodynamical and magneto-hydrodynamical accretion flows from a same thick torus around black holes show many similarities such as highly time-dependent accretion rate and Kelvin-Helmholtz instability in spite of the different mechanism of angular momentum transfer (Stone, Pringle & Begelman 1999; Stone & Pringle 2001). They also show that, for strong magnetic field, a small fraction of outflows near the pole is escaped as a powerful MHD wind, whereas the outflows in the hydrodynamical simulations are bound. This suggests that the unstable nature of the outflows from the thick accretion flow may be furthermore enhanced in 2D magneto-hydrodynamical simulation.

6 SUMMARY AND DISCUSSION

We examined the mass-outflow in the hot geometrically thick accretion flows such as the low angular momentum accretion flow and the advection-dominated accretion flow

around black holes, using 2D time-dependent HD calculations. The results are summarized as follows.

(1) In the low angular momentum flows, the inward accreting matter on the equatorial plane interacts with the outward moving gas and the centrifugally supported oblique shock is formed along the interface of both the flows provide the viscosity parameter α is as small as $\alpha \leq 10^{-3}$. The hot blobs, which lead to the eruptive mass-outflow, are generated at the inner shocked region and grow up toward the outer boundary.

(2) The advection-dominated accretion flows attain finally to a torus disc with the inner edge of the disc at $3 \leq r/R_g \leq 6$ and the center at $6R_g \leq r \leq 10R_g$. The hot blobs are formed near the inner edge of the torus disc and grow up along the outer surface of the disc.

(3) In both models, the mass-outflow is unstable and eruptive in nature. As a result, the luminosity and the mass-outflow rate are modulated irregularly and especially the relative modulation amplitudes $\delta\dot{M}_{\text{out}}/\dot{M}_{\text{out}}$ of the mass-outflow rate are as large as a few to ten.

(4) The origin of the unstable mass-outflow is ascribed to the Kelvin-Helmholtz instability which is ascertained by examining the Richardson number criterion (Eq. 14) for Kelvin-Helmholtz instability at the inner region of the flow.

(5) The flare phenomena of Sgr A* may be explained by the unstable mass-outflow examined here, together with the scenario of the temporal sequence of disc-jet coupling observed in the X-rays, IRs and radio wavelengths of the microquasar GRS 1915+105 (Mirabel et al. 1998).

The unstable mass-outflow seems to be inevitable as far as we consider the thick accretion flows with small angular momentum around the black holes. The present study shows that both the models of the low angular momentum accretion flow and the advection-dominated accretion flow produce the eruptive mass-outflows. These models would reproduce the reasonable spectra fitted to the observed ones of Sgr A* if we take in the appropriate model parameters, such as the accretion rate \dot{M} , the viscous parameter α , the magnetic field strength β and a hybrid electron population of thermal and nonthermal particles, following the idea and method described by Yuan, Quataert & Narayan (2003, 2004). Further, the evidence of angular momentum would confirm the validity of the models. Moreover, it is required to perform magneto-hydrodynamical research instead of only the hydrodynamical one. This is because the magnetic field will play important roles not only in the small-scale region of the accretion flow but also the large-scale of the interstellar space.

REFERENCES

- Abramowicz M. A., Czerny, B., Lasota, J. P., Szuszkiewicz, E., 1988, ApJ, 332, 646
- Abramowicz M. A., Igumenshchev, I. V., Quataert, E., Narayan, R., 2002, ApJ., 565, 1101
- Begelman, M. C., 2012, MNRAS, 420, 2912
- Blandford, R. D., Begelman, M., C., 1999, MNRAS, 303, L1
- Blandford, R. D., Begelman, M., C., 2004, MNRAS, 349, 68

- Bu, D., Yuan, F., Wu, M., Cuadra, J., 2013, MNRAS, 434, 1692
- Chandrasekhar S., 1961, Hydrodynamic and Hydromagnetic Stability, Oxford University Press, Oxford
- Czerny B., Mościbrodzka M., 2008, J. Phys. Conf. Ser., 131, 012001
- Eckart A., Schödel R., Meyer L., Trippe S., Ott T., Genzel R., 2006, A&A, 455, 1
- Esin A. A., Narayan R., Ostriker E., Yi I., 1996, ApJ, 465, 312
- Fukue, J., 1986, PASJ, 38, 167
- Genzel R., Schödel R., Ott T., Eckart A., Alexander T., Lacombe F., Rouan D., Aschenbach B., 2003, Nat, 425, 934
- Ghez A. M. et al., 2004, ApJ., 601, L159
- Igumenshchev, I. V., 2002, ApJ., 577, L31
- Li J., Ostriker J., Sunyaev R., 2013, ApJ., 767, 105
- Meyer L., Schödel R., Eckart A., Karas V., Dovčiak M., Duschl W.J., 2006a, A&A, 458, L25
- Meyer L., Eckart A., Schödel R., Duschl W.J., Mužić K., Dovčiak M., Karas, V., 2006b, A&A, 460, 15
- Mirabel L. F., Dhawan V., Chaty S., Rodríguez L. F., Martí J., Robinson C. R., Swank J., Geballe T. R., 1998, A&A, 330, L9
- Mościbrodzka M., Das T.K., Czerny B., 2006, MNRAS, 370, 219
- Narayan R., Igumenshchev, I. V., Abramowicz, M. A., 2000, ApJ., 539, 798
- Narayan, R., Sądowski, A., Penńa, R.F., Kurkarni, A.K., 2012, MNRAS, 426, 3241
- Narayan R., Yi I., 1994, ApJ, 428, L13
- Narayan R., Yi I., 1995, ApJ, 452, 710
- Okuda T., 2014, MNRAS, 441, 2354
- Okuda T., Molteni D., 2012, MNRAS, 425, 2413
- Okuda T., Fujita M., Sakashita S., 1997, PASJ, 49, 679
- Okuda T., Lipunova G. V., Molteni D., 2009, MNRAS, 398, 1668
- Okuda T., Teresi V., Molteni D., 2007, MNRAS, 377, 1431
- Quataert, E., Gruzinov, A., 2000, ApJ., 539, 809
- Shakura N.I., Sunyaev R.A., 1973, A&A, 24, 337
- Shu F. H., 1992, Osterbrock D. E., Miller J. S., eds., The Physics of Astrophysics, Volume II: Gas Dynamics, University Science Books, California
- Stone J. M., Pringle, J. E., 2001, MNRAS, 322, 461
- Stone J. M., Pringle, J. E., Begelman, M. C., 1999, MNRAS, 310, 1002
- Stepney S., Guilbert P.W., 1983, MNRAS, 204, 1269
- Trippe S., Paumard T., Ott T., Gillessen S., Eisenhauer F., Martins F., Genzel, R., 2007, MNRAS, 375, 764
- Yuan F., 2011, in Morris M.R., Wang Q.D., Yuan F., eds, ASP Conf. Ser. 439, The Galactic Center: A Window to the Nuclear Environment of Disk Galaxies. Astron. Soc. Pac., San Francisco, p. 346
- Yuan, F., Bu, D., Wu, M., 2012, ApJ., 761, 130
- Yuan F., Gan, Z., Narayan, R., Sądowski, A., Bu, D., Bai, X.N., 2015, ApJ., 804, 101
- Yuan, F., Lin, J., Wu, K., Ho, L. C., 2009, MNRAS, 395, 2183
- Yuan F., Narayan R., 2014, ARA&A, 52, 529
- Yuan F., Quataert E., Narayan R., 2003, ApJ, 598, 301
- Yuan F., Quataert E., Narayan R., 2004, ApJ, 606, 894
- Yuan F., Wu M., Bu D., 2012, ApJ, 761, 129
- Yusef-Zadeh F. et al., 2009, ApJ, 706, 348
- Yusef-Zadeh F., Wardle M., Miller-Jones J.C.A., Roberts D.A., Grosso N., Porquet D., 2011, ApJ, 729, 44